Plasmonics
https://doi.org/10.1007/s11468-025-03087-0

RESEARCH

High-Surface-Sensitive Self-Referenced Plasmonic Sensor Based on Au Nanoislands

Kimberly Melgarejo[1,3] · Melisa del Barrio[2] · Elena Benito-Peña[2] · Teona Mirea[1] · Carlos Angulo Barrios[3]

Received: 6 April 2025 / Accepted: 28 May 2025

Abstract

We present a self-referenced plasmonic sensor with a high surface sensitivity based on Au nanoislands synthesized by thermal dewetting on a planar SiO_2/metal bilayer deposited on a Si chip. The optical device displays two spectral features in reflection: a Fabry-Pérot resonance due to the SiO_2/metal bilayer and a localized surface plasmon resonance (LSPR) associated with the Au nanoislands, serving as a reference and sensing signal, respectively. Surface sensitivity was investigated through the study of bovine serum albumin protein adsorption. The device exhibited a surface sensitivity of 0.2 nm/(ng/cm^2), an order of magnitude greater than other plasmonic devices based on Au nanoislands. The device response was theoretically modeled using rigorous coupled-wave analysis (RCWA) simulations, which showed strong agreement with the experimental results and provided design guidelines for further sensitivity improvement. The combination of high surface sensitivity, chip-based architecture, cost-effectiveness, and a straightforward Au nanostructure synthesis procedure positions this device as a promising self-referenced plasmonic sensor for biosensing applications.

Keywords Optical biosensor · Surface sensing · Localized surface plasmon resonance · Metal nanoparticle · Protein adsorption

Introduction

Metal nanoparticles, particularly noble metals like gold and silver, exhibit collective oscillation of conductive electrons when stimulated by visible light, a phenomenon known as localized surface plasmon resonance (LSPR). The LSPR condition is influenced by the local dielectric environment; thus, when biomolecules (e.g., proteins, DNA, or antigens) bind to the nanoparticle surface, they induce a change in the local refractive index, leading to a shift in the LSPR wavelength. This spectral shift can be easily monitored using conventional readout instrumentation, offering a direct, label-free method for detecting biomolecular interactions. This principle has guided the development of numerous plasmonic biosensors that utilize metal nanostructures and have been demonstrated in various forms [1]. These include both colloidal solutions of metal nanoparticles [2–5] and chip-based designs, where nanostructures or nanoparticles are attached to a planar substrate [6–17].

The fabrication of LSPR-based sensors onto a chip offers distinct advantages, including the capacity for multiplexed analysis and seamless integration with electronic and microfluidic systems. Chip-based LSPR sensors can be fabricated using both lithography-based and lithography-free approaches. Lithography-based techniques, such as electron beam lithography [6] and nanoimprint lithography [7], enable precise control over the positioning and dimensions of nanostructures according to predefined patterns. However, these methods typically require numerous processing steps and sophisticated, high-cost equipment. Conversely, lithography-free nanofabrication processes, such as colloidal nanoparticle deposition [8–11] and dewetting [12–19], often yield a low-ordered or random distribution of

✉ Teona Mirea
teona.mirea@upm.es

✉ Carlos Angulo Barrios
carlos.angulo.barrios@upm.es

[1] Department of Electronic Engineering, CEMDATIC, ETSI Telecomunicación, Universidad Politécnica de Madrid, Ciudad Universitaria s/n, Madrid 28040, Spain

[2] Department of Analytical Chemistry, Faculty of Chemistry, Universidad Complutense, Madrid 28040, Spain

[3] Department of Photonics and Bioengineering, CEMDATIC, ETSI Telecomunicación, Universidad Politécnica de Madrid, Ciudad Universitaria s/n, Madrid 28040, Spain

Published online: 04 June 2025

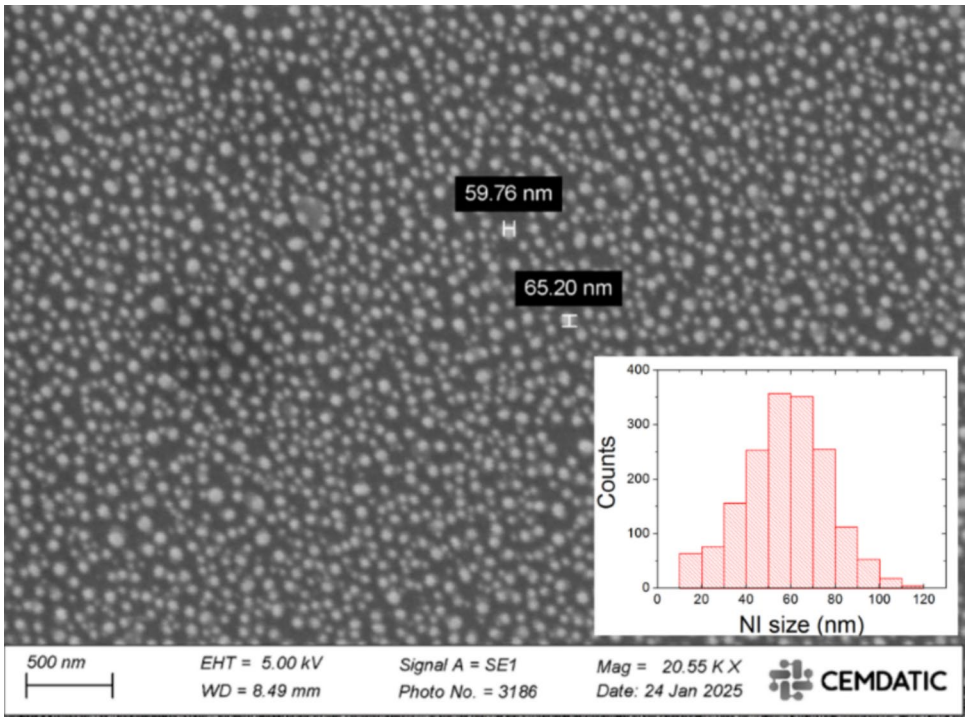

Fig. 1 Scanning electron microscope image of the top view of the fabricated device. Inset shows a histogram of the particle size distribution

nanoparticles, exhibiting significant size dispersion. However, these processes are more straightforward and cost-effective. In particular, thermal dewetting by annealing of thin metal films is considered to be among the simplest and most economical methods for producing metal nanostructures on solid substrates. The dewetting or agglomeration of a thin metal layer occurs during the annealing process at a temperature below the metal's melting point, while the film remains in a solid state, resulting in the formation of metal nanostructures, commonly known as nanoislands (NIs) [12]. Dewetting of NIs from thin metal films can be achieved at the wafer level in a massively parallel manner, exhibiting substrate-dependent plasmonic phenomena across a broad spectral range, from the ultraviolet to the infrared [17].

Recently, we demonstrated a self-reference plasmonic refractometric sensor based on Au NIs synthesized by thermal dewetting on a planar SiO_2/metal/Si chip [20]. The device's reflectance was attributed to the result of combining two resonance phenomena: a Fabry-Pérot resonance associated with the SiO_2/metal nanocavity and an LSPR related to the Au NIs. The Fabry-Pérot resonance demonstrated minimal sensitivity to bulk refractive index variations, thus serving as a reference signal, whereas the LSPR exhibited a notable sensitivity to such variations, thereby functioning as the sensing signal. The device achieved a bulk refractive index sensitivity of 212 nm/refractive index unit (RIU), surpassing that of analogous configurations based on Au nanoparticles deposited on planar substrates, while additionally providing self-referencing capabilities. To the best of our

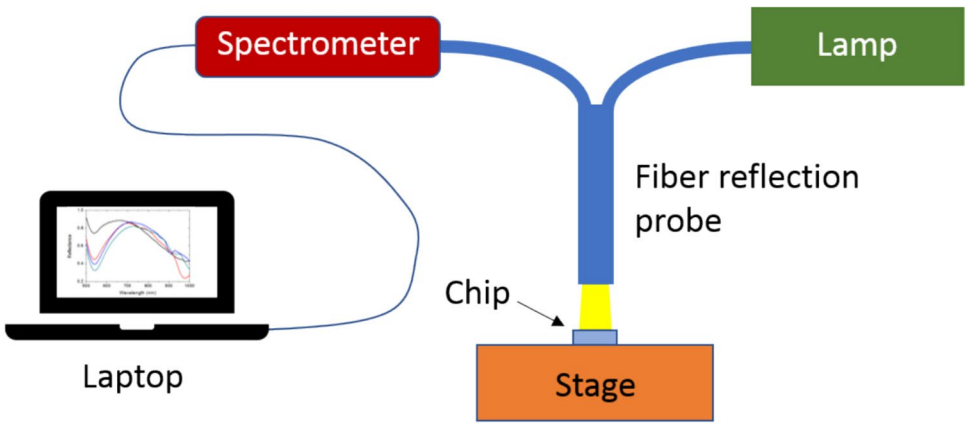

Fig. 2 Schematic diagram of the spectral reflectance characterization setup

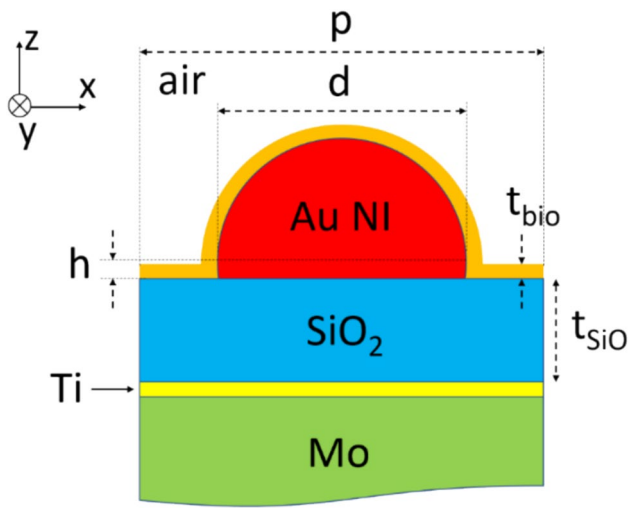

Fig. 3 Schematic diagram of the unit cell of the simulated device. The device is modeled as a square array of period *p*, composed of spherical caps of Au (nanoislands) with a diameter of *d*

knowledge, this was the first demonstration of a self-referencing feature in a refractive index sensor based on metal NIs. In comparison to other self-referenced refractive index plasmonic sensors [21–26] that also rely on the generation of independent multiple resonances with different sensitivities to the refractive index of the analyte, our sensor offers a simple design that can be easily fabricated for generating the reference signal.

The objective of this work is to further investigate the sensing performance of the configuration described in [20]. The study encompasses both experimental and theoretical assessments of bovine serum albumin (BSA) protein adsorption, with the aim of determining the configuration's surface sensitivity. Surface sensitivity is a key parameter for affinity-based biosensors, and BSA serves as an ideal standard test molecule to determine the surface sensitivity and detection limits of nanoparticle-based sensors. BSA is a well-characterized protein with a known molecular weight (~66.5 kDa), stable tertiary structure, and consistent adsorption behavior. BSA adsorption experiments are simple, reproducible, and cost-effective and provide direct insights into nanoparticle surface interactions, especially for biosensing applications. Consequently, the analysis of metal nanoparticle responses to BSA adsorption offers valuable insights into their potential for detecting other biomolecules, including disease markers, toxins, and pathogens in diagnostic applications. The theoretical analysis was conducted using rigorous coupled wave analysis (RCWA) calculations and aimed to evaluate the effectiveness of a simplified device model in analyzing the sensor response.

Experimental

Au nanoislands were synthesized on a SiO_2/Ti/Mo multilayer structure through thermal annealing. First, the multilayer was formed on a Si substrate by sequentially depositing

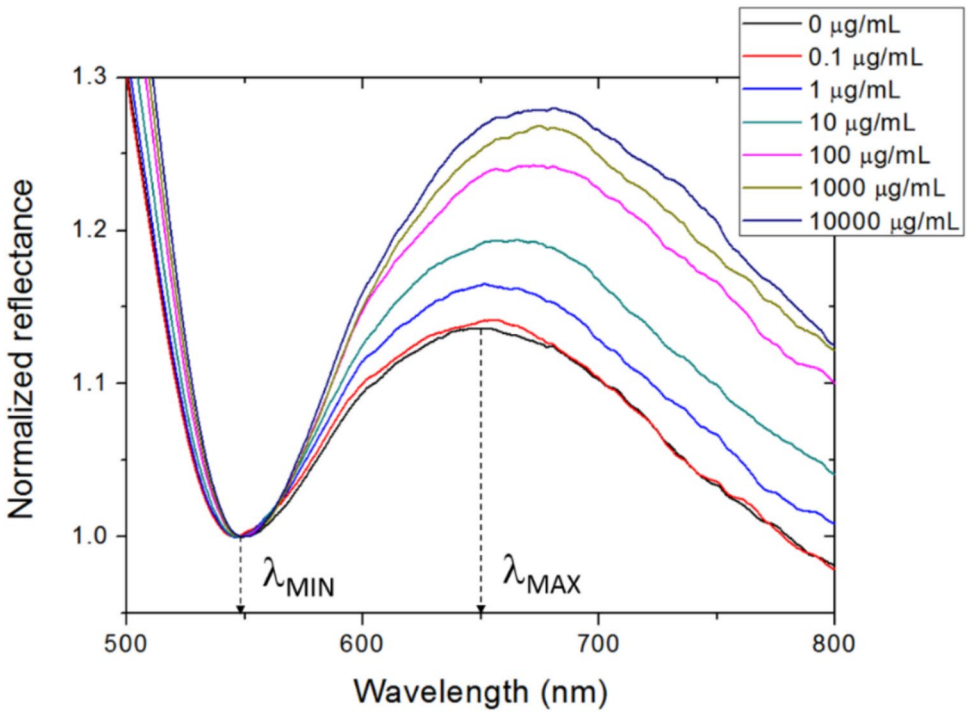

Fig. 4 Measured spectral reflectance of the fabricated device after BSA incubations at various concentrations. The curves are normalized to the corresponding reflectance value at λ_{MIN}

a)

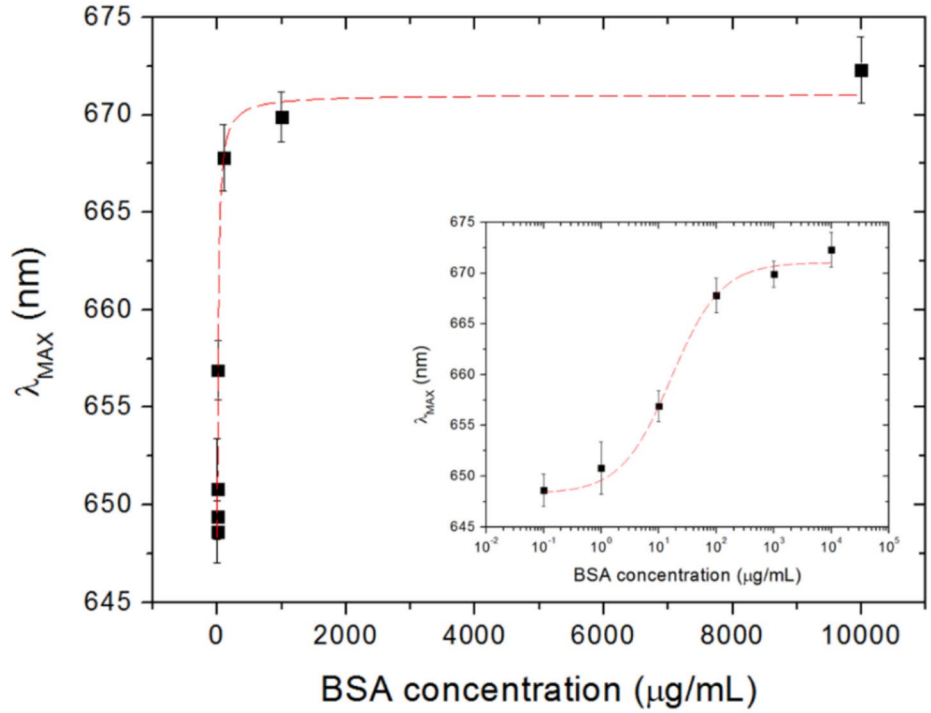
675
670
665
660
655
650
645
λ_{MAX} (nm)
0
2000
4000
6000
8000
10000
BSA concentration (μg/mL)
λ_{MAX} (nm)
BSA concentration (μg/mL)

b)

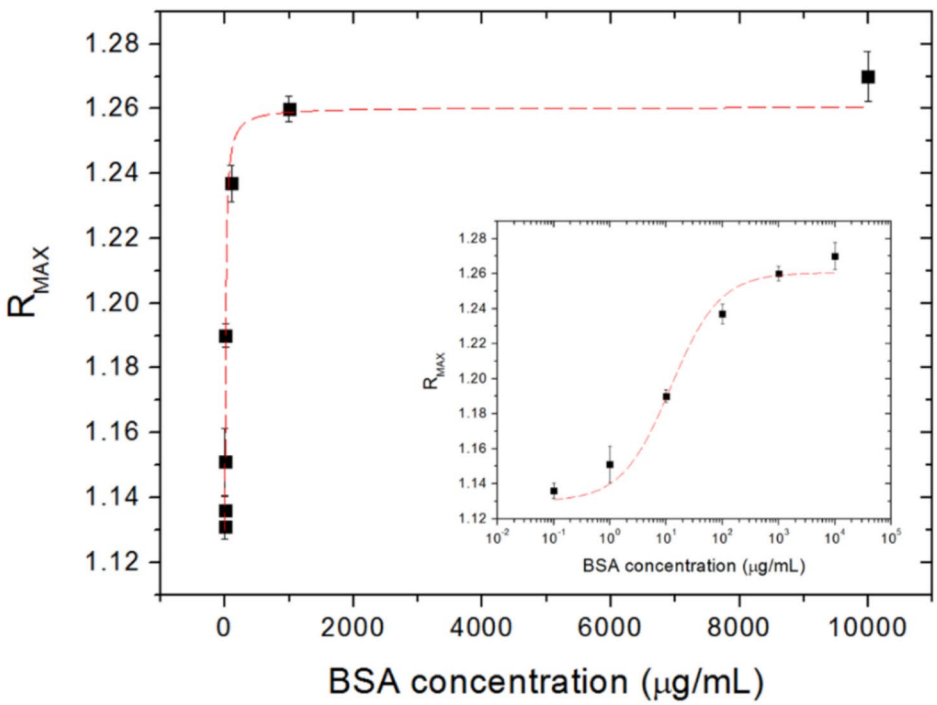
1.28
1.26
1.24
1.22
1.20
1.18
1.16
1.14
1.12
R_{MAX}
0
2000
4000
6000
8000
10000
BSA concentration (μg/mL)
R_{MAX}
BSA concentration (μg/mL)

◂**Fig. 5** Calibration graphs of the fabricated device. **a** λ_{MAX} and **b** R_{MAX} as a function of BSA concentration. Insets show semi-logarithmic representation of the measured data. Dashed red lines represent Langmuir fittings of the data points. Error bars represent ± standard deviation, derived from three reproducibility measurements

a 10-nm-thick Ti layer, a 150-nm-thick Mo layer, a 10-nm-thick Ti layer, and a 100-nm-thick SiO_2 layer. The deposition of these layers was carried out using a DC-pulsed reactive sputtering system, with power settings adjusted to 150 W for Ti, 400 W for Mo, and 1200 W for SiO_2, respectively. The sputtering parameters included an oxygen pressure of 5.4 mBar for Ti, 0.7 mBar for Mo, and 3.3 mBar for SiO_2. Subsequently, a 5-nm-thick Au film was deposited onto the SiO_2 layer by sputtering. Finally, thermal annealing was performed in a quartz oven at 545 °C for 1 h in an air atmosphere. Figure 1 shows a top-view scanning electron microscope (SEM) image of the resulting Au NIs and their size distribution (inset). By using ImageJ software, the mean size of the Au NIs was determined to be approximately 60 nm (inset) with a surface density of approximately 95 nanoparticles/μm^2. Information regarding the reproducibility of the fabrication method can be found in the Supplementary Information (SI.1).

The sample chip was optically characterized in reflection mode, as schematically shown in Fig. 2. A tungsten-halogen lamp (Thorlabs SLS201L) was coupled to one end of a bifurcated fiber reflection probe (Ocean Optics R200-7-VIS–NIR), which perpendicularly illuminated the surface of the sample containing the Au NIs. The light reflected from the device was collected by the fiber reflection probe, whose second end was connected to a spectrometer (CC200 Thorlabs) to measure the spectral distribution of the reflected light. Spectral reflectance was calculated by dividing the measured spectral distribution of the reflected light from the sample by that from an aluminum mirror.

A series of protein adsorption measurements were conducted to assess the surface sensitivity of the fabricated device. First, the device chip was cleaned with ethanol (≥ 99.5% purity) for 2 min and dried under a nitrogen flow. Then, the chip was exposed to a series of incubations with aqueous solutions of BSA (≥ 96%, Sigma Aldrich), at concentrations ranging from 0.1 to 10,000 μg/mL in tenfold increments. These incubations were performed by depositing 50 μL of BSA solution onto the device surface for 1 h at room temperature in a humidified chamber to prevent evaporation. After the incubation period, the device chip was rinsed twice with distilled water and dried with nitrogen, and then its spectral reflectance was measured. To evaluate reproducibility, the optical response of the device was measured following the removal and repositioning of the chip onto the stage three times.

Simulations

The structure under consideration was modeled as a square array of period p composed of solid spherical caps of Au with a diameter of *d*, positioned on a SiO_2 layer of thickness $t_{SiO} = 100$ nm. Figure 3 presents a schematic representation of the array unit cell. The SiO_2 layer, in turn, is located on a 10-nm-thick Ti layer, which is deposited on a semi-infinite Mo substrate. The diametral plane of the Au spherical caps is separated from the SiO_2 layer by a distance *h*. A biolayer with a refractive index of 1.4 and a thickness of t_{bio} is assumed to be conformably adsorbed onto the device surface. The entire structure is surrounded by air. The frequency-dependent dielectric constants of Au, SiO_2, Ti, and Mo were modeled by the well-known Drude-Lorentz equation, with the fitted parameters reported in the literature [27–29]. The optical reflectance versus wavelength was calculated by using the 3D rigorous coupled-wave analysis (RCWA) method (from Rsoft

Table 1 Comparison of the gold nanoisland platform studied in this work with other plasmonic nanostructures for surface sensing based on cost-effective fabrication methods reported in the literature. In all cases, BSA adsorption is used to experimentally evaluate surface sensitivity

Type of substrate	Nanostructure synthesis	BSA concentration (mg/mL)	Peak shift (nm)	Surface sensitivity (nm cm^2 ng^{-1})[(1)]	Ref
Au nanohole	Colloidal lithography	10	7	0.06	[38]
Au nanohole	Interference lithography	1	1.6	0.01	[39]
Au nanodisk	Colloidal lithography	6.64	0.7	0.006	[40]
Au nanoribbon	Soft lithography	6.64	1	0.009	[41]
Au-coated nanograting	Nanoimprint lithography	33	3.5	0.03	[42]
Au nanoparticle	Turkevich method	3.3	7.4	0.07	[43]
Au nanoisland	Thermal dewetting	6.64	8.9	0.08	[35]
Au nanoisland	Thermal dewetting	1	22	0.2	This work

[(1)]Assuming a BSA surface mass density of 110 ng/cm^2 [44]

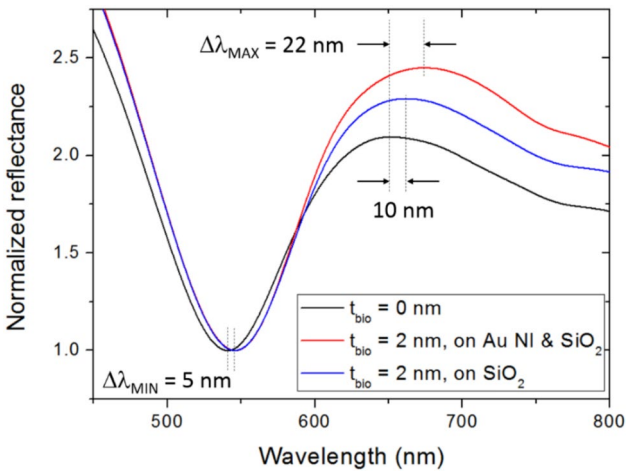

Fig. 6 Calculated response curves of the modeled device for $p = 100$ nm, $d = 60$ nm, and $h = 10$ nm. Black line corresponds to the baseline ($t_{bio} = 0$ nm). Red and blue lines correspond to a biolayer thickness of 2 nm on the Au NIs and the SiO_2 surface and only on the SiO_2 surface, respectively

Components Design Suite), which is a powerful numerical technique used to solve Maxwell's equations for electromagnetic wave interaction with periodic structures.

Results and discussion

Figure 4 illustrates the measured spectral responses of the fabricated sensor for the considered BSA concentrations within the spectral range of 500–800 nm. All curves exhibit a dip at a wavelength of approximately 550 nm and a broad peak at longer wavelengths. The curves in Fig. 4 are normalized with respect to the corresponding reflectance value of the dip. As discussed in [20], the spectral dip is attributed to a Fabry–Pérot resonance associated with the SiO_2/metal planar nanocavity, while the peak is attributed to a LSPR related to the Au NIs. It is seen that the spectral position of the dip remains largely unaltered by the BSA incubation experiments, making it a stable reference signal. In contrast, the spectral peak undergoes a clear redshift as the BSA concentration increases, rendering it suitable as a surface sensing signal. This behavior of both resonance features is consistent with the results reported in [20] for a bulk refractive index sensitivity study.

Figure 5a and b shows the spectral position (λ_{MAX}) and normalized reflectance (R_{MAX}) of the maximum of the LSPR band, respectively, as a function of the BSA concentration. To determine the values of λ_{MAX} and R_{MAX}, the measured curves were fitted to a 3-order polynomial function, as described in the Supplementary Information (SI.2). The data points in Fig. 5 were fitted to a Langmuir isotherm function of the form:

$$y(c) = y_b + \frac{(y_m - y_b)Kc}{1 + Kc} \quad (1)$$

where y_m and y_b are the maximum and minimum values of the sensor response, c is the BSA concentration and K is the Langmuir equilibrium constant. The adjusted correlation coefficient (Adj. R^2) values for the fittings were 0.9920 and 0.9913 for λ_{MAX} and R_{MAX}, respectively. The K values obtained from the fittings were 64 mL/mg and 78 mL/mg for λ_{MAX} and R_{MAX}, respectively. The similarity of these K values indicates that both λ_{MAX} and R_{MAX} monitoring can be used to determine this relevant parameter, which is a measure of the affinity between the adsorbate and the surface. For the sake of comparison, the equilibrium constant for BSA adsorption on colloidal nanopore silica particles was reported to range from 2.6 mL/mg to 9.4 mL/mg [30], whereas the equilibrium constant for BSA adsorption on colloidal gold particles was determined to be in the range from 7.7 mL/mg (0.51×10^6 L/mol) to 25 mL/mg (1.65×10^6 L/mol) [31]. These K values are lower than those obtained in this work, which can be attributed to the enhanced molecular spreading and increased interaction sites afforded by a flat surface, thereby elevating the adsorption affinity. Moreover, the immediate availability of adsorption sites on a planar

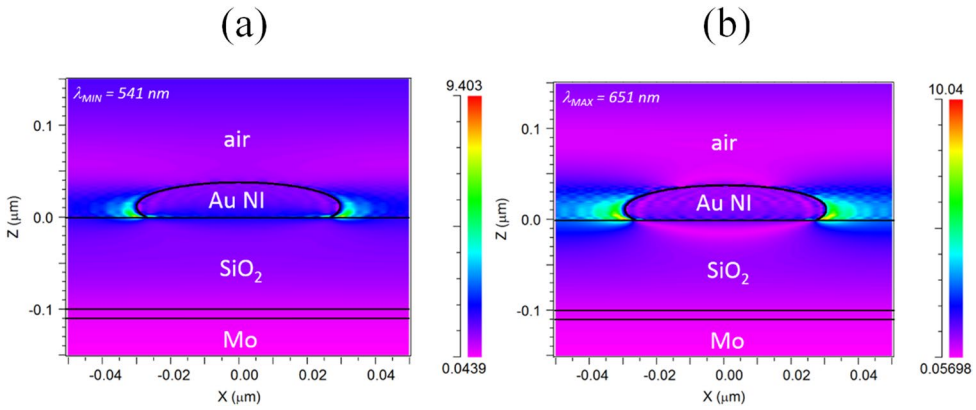

Fig. 7 Calculated x-component of the electric field (E_x) distribution at **a** $\lambda_{MIN} = 541$ nm and **b** $\lambda_{MAX} = 651$ nm of the modeled Au NI/SiO_2/Ti/Mo configuration in the XZ plane ($Y = 0$). $d = 60$ nm, $p = 100$ nm, $h = 10$ nm, and $t_{bio} = 0$

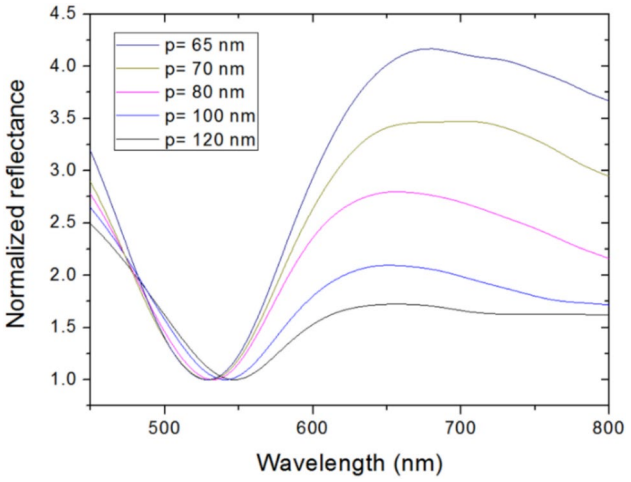

Fig. 8 Computed response curves of the modeled device for $d = 60$ nm, $h = 10$ nm, $t_{bio} = 0$ m, and different values of p

surface is advantageous. In contrast, aggregation or protein–protein interactions in colloidal nanoparticles can hinder accessibility to adsorption sites, which may account for the observed differences.

It should be noted that the previous Langmuir fitting assumed the formation of a monolayer of BSA molecules on the sensor surface. As illustrated in Fig. 5, both λ_{MAX} and R_{MAX} attain saturation, suggesting complete surface coverage by protein molecules, at approximately 1 mg/mL of BSA. This finding aligns with the observations reported by other researchers regarding BSA protein adsorption on various surfaces [32–34], which indicate that a monolayer of BSA forms during incubations at low concentrations (≤ 1 mg/mL) while multilayers may develop at higher BSA concentrations. Therefore, the assumption of monolayer formation for the Langmuir fitting is well supported.

The limit of detection (LOD) is typically defined as $LOD = 3\sigma_b/S$, where σ_b is the standard deviation of the baseline ($c = 0$) and S is the sensitivity. In the present study, the standard deviation values of the baseline were measured to be 1.1 nm and 0.00369 for λ_{MAX} and R_{MAX}, respectively. The sensitivity can be estimated by calculating the slope of the Langmuir fit functions at $c = 0$, resulting in 0.86 nm/(μg/mL) and 0.0059 /(μg/mL) for λ_{MAX} and R_{MAX}, respectively. Consequently, the LOD values corresponding to λ_{MAX} and R_{MAX} monitoring are 4 μg/mL and 2 μg/mL, respectively.

In order to compare the surface-sensing performance of the presented sensor with other plasmonic sensors, the use of the sensitivity in terms of volumetric density of solute might not be adequate, as these parameters may vary depending on variables such as incubation time, solvent type, and solute type. Instead, the use of the surface sensitivity for the same adsorbate (BSA), defined as $S_\Gamma = (\Delta\lambda_{MAX})_S/\Gamma$, where $(\Delta\lambda_{MAX})_S$ is λ_{MAX} variation at signal saturation and Γ is the surface mass density of a monolayer of BSA, offers a suitable metric for comparison. Table 1 compiles data on plasmonic nanostructure-based surface sensors fabricated using cost-effective methods. As shown, the device described in this study exhibits the highest surface sensitivity (LSPR wavelength shift interrogation). Specifically, the surface sensitivity of our device is one order of magnitude greater than that reported for another comparable plasmonic sensor chip based on Au NIs [35]. This enhancement can be attributed to the fact that our device operates in reflection mode, whereas the device reported in [35] works in transmission mode. In reflection mode, light passes through the nanoplasmonic sensing layer twice before reaching the spectrometer, resulting in higher light-matter interaction and higher detection sensitivity [36, 37].

Figure 6 shows the RCWA-calculated reflectance curves of the modeled device for $d = 60$ nm, $p = 100$ nm, $h = 10$ nm, and $t_{bio} = 0$ (black line) and $t_{bio} = 2$ nm (red line). Note that the simulated curves exhibit comparable spectral characteristics to the experimental device. The values of d and p were determined from the mean NI diameter and density ($= 1/p^2$), respectively, obtained from the SEM characterization of the actual sample. The value of h is related to the contact angle of the NI with respect to the substrate and can largely determine the LSPR wavelength [17]. In the present study, the h value was adjusted such that the λ_{MIN} and λ_{MAX} values of the simulated curve coincide approximately with those of the experimental curve (see SI.3 of the Supplementary Information for details). Figure 7a and b depicts the calculated x-component of the electric field (E_x) distributions for the Au NI/SiO_2/Ti/Mo configuration ($t_{bio} = 0$) at $\lambda_{MIN} = 541$ nm and $\lambda_{MAX} = 651$ nm, respectively. As illustrated in Fig. 7a, the field intensity profile at $\lambda_{MIN} = 541$ nm experiences a monotonic decay within the SiO_2 layer, a phenomenon that is characteristic of an anti-symmetric Fabry–Pérot resonance [45]. The absence of nodes indicates that only the lowest order Fabry–Pérot mode is involved. Figure 7b shows that the E_x intensity at

Table 2 Calculated $\Delta\lambda_{MAX}$ and ΔR_{MAX} for a biolayer of thickness $t_{bio} = 2$ nm adsorbed on the whole device surface, $d = 60$ nm, $h = 10$ nm, and various values of p

p (nm)	Density (NI/μm^2)	$\Delta\lambda_{MAX}$ (nm)	ΔR_{MAX}
120	69	9.3	0.2853
100	100	22	0.3541
80	156	29	0.6169
70	204	LSP band not well defined	LSP band not well defined
65	237	LSP band not well defined	LSP band not well defined

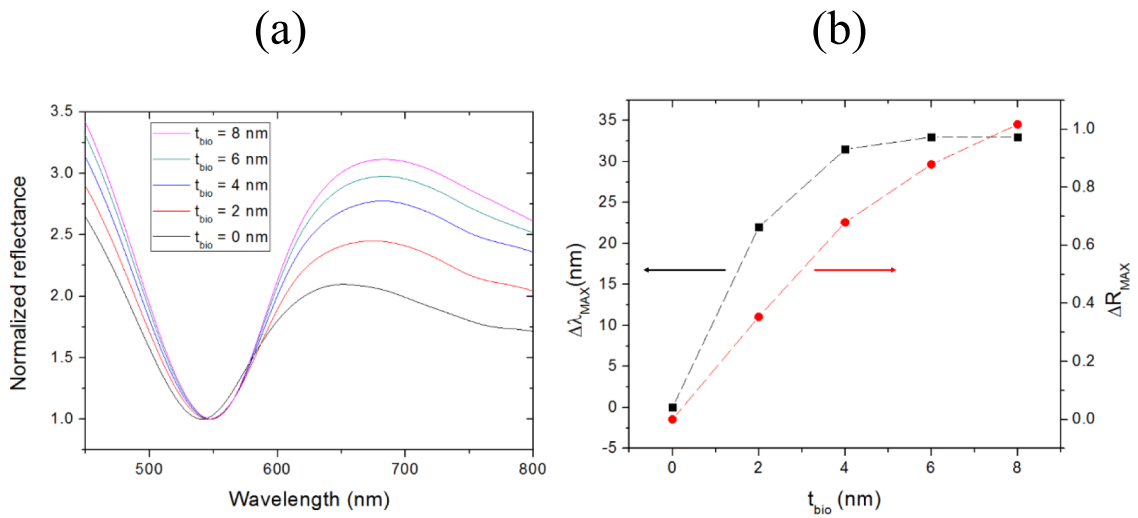

Fig. 9 **a** Computed response curves of the modeled device for $d = 60$ nm, $h = 10$ nm, $p = 100$ nm, and different values of t_{bio}. **b** Variations of λ_{MAX} (black squares) and R_{MAX} (red circles) with respect to the baseline ($t_{bio} = 0$ nm) as a function of t_{bio}

$\lambda_{MAX} = 651$ nm experiences significant enhancement along the right and left edges of the Au NI, indicative of the characteristic behavior of an LSP resonance.

The biolayer thickness has been assumed to be 2 nm, which is a typical value for a BSA monolayer under dry conditions [34, 46]. As shown in Fig. 6, the calculated LSPR wavelength shift, $\Delta\lambda_{MAX}$, is found to be 22 nm, which is significantly greater than the dip shift ($\Delta\lambda_{MIN} = 5$ nm) and equivalent to that measured for the actual device. This similarity indicates that the proposed model is suitable for simulating the device's response regarding wavelength shift. This represents a significant outcome, as it considerably simplifies the theoretical analysis of the device and the designer's tasks. Specifically, the optical response of randomly distributed, varying-sized Au NIs can be modeled with good accuracy by simulating a straightforward periodic arrangement of single-sized Au NIs. Concerning the reflectance response (R_{MAX}), the simulated ΔR_{MAX} value equals 0.3541, which is greater than the experimental value (0.1336). This discrepancy is attributed to the fact that the surfaces of the actual device are not perfectly smooth, which induces light scattering and decreases the reflectance in the direction normal to the device. However, the simulations indicate a substantial increment in the R_{MAX} value after the adsorption of the biolayer, in good agreement with the experimental results.

We also simulated the device response under the assumption that BSA adsorption occurs only on the SiO_2 surface (blue line in Fig. 6). The resulting curve exhibits a dip that coincides with that of the red line (BSA on the entire device surface), indicating that the deposition of BSA molecules on the SiO_2 is responsible for the small shift of λ_{MIN}. It is also noted that BSA adhesion on the SiO_2 surface produces a redshift of λ_{MAX} equal to 10 nm, significantly contributing to the overall redshift of λ_{MAX} when BSA adheres to the whole device surface. The observed shift in λ_{MAX} due to BSA on the SiO_2 surface can be attributed to an increase in both the local refractive index surrounding the Au NIs and coupling effects between neighboring NIs due to the presence of a higher-index material between them [17].

The impact of the biolayer deposited on the SiO_2 surface on the overall λ_{MAX} shift is notable. However, as illustrated in Fig. 6, the predominant contribution to the overall λ_{MAX} shift is attributable to the biolayer covering the Au NIs. This suggests that a higher density of NIs should lead to a higher surface sensitivity. To corroborate this, a series of simulations were conducted for several p values, that is, different NI densities. Table 2 shows the calculated $\Delta\lambda_{MAX}$ and ΔR_{MAX} for an adlayer covering the whole device surface, $d = 60$ nm, $h = 10$ nm, and several values of p. As expected, both $\Delta\lambda_{MAX}$ and ΔR_{MAX} increase with decreasing period (increasing density). However, for periods ≤ 70 nm, the corresponding LSP band broadens and shows small bumps, which complicates the determination of the spectral position of λ_{MAX}. This is illustrated in Fig. 8, which shows the calculated normalized reflectance for $d = 60$ nm, $h = 10$ nm, $t_{bio} = 0$ nm, and various p values ranging from 120 to 65 nm. The presence of these bumps is attributed to coupling effects between the NIs as the distance between them decreases [17]. The imprecision in determining the peak of the LSP band in high-density NI configurations may complicate the interpretation of the sensor response, thereby hindering its suitability for quantitative applications. According to the results of our simulations, a p value of 80 nm (156 NI/μm^2) provides the highest surface sensitivity while allowing a facile determination of the LSPR maximum. Subsequent research

endeavors will center on synthesizing Au NIs with this density to further enhance surface sensitivity. The predicted sensitivity behavior with p (density) was supported experimentally by characterizing another fabricated sample with the same mean NI diameter (60 nm) but with smaller NI density (80 NI/μm^2) (see SI.4 of the Supplementary Information for details). That sample exhibited a $\Delta\lambda_{MAX}$ of approximately 15 nm, in good agreement with the calculated results presented in Table 2.

Figure 9a shows the calculated sensor response for varying values of the biolayer thickness (t_{bio}), ranging from 0 to 8 nm. The peak wavelength shift ($\Delta\lambda_{MAX}$) and reflectance variation (ΔR_{MAX}) as a function of t_{bio} are plotted in Fig. 9b. It is observed that $\Delta\lambda_{MAX}$ increases significantly with t_{bio} for small values of t_{bio} and saturates at approximately $t_{bio} = 6$ nm, indicating a small decay length of the evanescent field associated with the LSPR [18]. This makes wavelength interrogation an effective method for using the proposed sensor for highly sensitive detection of thin (a few nanometers thick) adlayers, but not for tens of nanometers thick films. ΔR_{MAX} also exhibits high sensitivity to t_{bio} but appears to saturate at higher values of t_{bio} as compared to $\Delta\lambda_{MAX}$. This can be attributed to the effect of the Fabry-Pérot cavity optical response on R_{MAX}. As t_{bio} increases, the device's top surface becomes flatter, reducing optical losses due to surface scattering and leading to a deeper and higher contrast Fabry–Perot resonance (R_{MAX} increases). R_{MAX} tends to saturate as a completely flat surface is approached. This result suggests that when detecting thick films, reflectance interrogation may be a more suitable method than wavelength interrogation because it covers a broader thickness dynamic range.

As illustrated in Fig. 5, both the measured λ_{MAX} and R_{MAX} exhibit small increments for [BSA] = 10 mg/mL in comparison to [BSA] = 1 mg/mL. If additional layers of BSA were formed for [BSA] = 10 mg/mL, the slight increase in λ_{MAX} could be explained by the onset of signal saturation observed in Fig. 9b. However, Fig. 9b also shows that the formation of additional layers of BSA would result in a substantially larger variation of R_{MAX} than that obtained experimentally. This suggests that no well-defined additional layers of BSA are formed for 10 mg/mL of BSA, and thus supports the preceding assertion that the sensor signal saturation observed in Fig. 5 is predominantly attributable to the establishment of a monolayer of BSA. The moderate increase in λ_{MAX} and R_{MAX} may be due to the compaction of the BSA monolayer or the formation of loosely packed protein aggregations on its surface.

Conclusions

The surface sensitivity of a self-referenced nanoplasmonic sensor based on Au NIs has been investigated through both BSA protein adsorption experiments and RCWA simulations. The Au NIs were synthesized by thermal dewetting on a planar SiO_2/metal/Si chip, and their spectral response was examined in reflection mode. The analytical signal of the sensor was studied in terms of LSPR spectral shift and normalized reflectance monitoring. Both measurements yield similar values for the BSA adsorption equilibrium constant and limit of detection. The device exhibits a surface sensitivity of 0.2 nm/(ng/cm^2) using wavelength shift monitoring, which is one order of magnitude greater than that of other plasmonic devices based on Au nanoislands. RCWA simulations of a periodic array of Au NIs closely resemble the experimental response of the device, validating the efficacy of the proposed simplified model. This model has been employed to determine an optimal value for the Au NI surface density to achieve both high surface sensitivity and precise LSPR band definition. The high surface sensitivity of the studied device, along with its chip-based architecture, low cost, and simplicity, makes it a promising self-referenced plasmonic sensor for biosensing applications.

Supplementary Information The online version contains supplementary material available at https://doi.org/10.1007/s11468-025-03087-0.

Acknowledgements The authors thank Ricardo Hervás García for his assistance during device fabrication.

Author Contributions C.A.B., T.M., M.B, and E.B.P. performed the study conception and design. Device fabrication and experimental characterization were performed by K.M. Data collection and analysis were performed by K.M and C.A.B. Numerical simulations and analysis were performed by C.A.B. The first draft of the manuscript was written by C.A.B. and all authors commented on previous versions of the manuscript. All authors read and approved the final manuscript.

Funding Open Access funding provided thanks to the CRUE-CSIC agreement with Springer Nature. This research was funded by the R&D National Plan of the Spanish Government (PID-2020-118410RB-C22, PID2021-127457OB-C21), UPM-INDRA Chair in Microelectronics-CHIP, and by the Comunidad de Madrid through the call Research Grants for Young Investigators from Universidad Politécnica de Madrid.

Data Availability The datasets generated and/or analyzed during the current study are available from the corresponding author on reasonable request.

Declarations

Ethics Approval Not applicable.

Consent to Participate Not applicable.

Consent for Publication Not applicable.

Competing interests The authors declare no competing interests.

References

1. Mayer KM, Hafner JH (2011) Localized surface plasmon resonance sensors. Chem Rev 111(6):3828–3857
2. Potara M, Gabudean AM, Astilean S (2011) Solution-phase, dual LSPR-SERS plasmonic sensors of high sensitivity and stability based on chitosan-coated anisotropic silver nanoparticles. J Mater Chem 21(11):3625–3633
3. Kreuzer MP, Quidant R, Salvador JP, Marco MP, Badenes G (2008) Colloidal-based localized surface plasmon resonance (LSPR) biosensor for the quantitative determination of stanozolol. Anal Bioanal Chem 391:1813–1820
4. Unser S, Bruzas I, He J, Sagle L (2015) Localized surface plasmon resonance biosensing: current challenges and approaches. Sensors 15(7):15684–15716
5. Huang H, Tang C, Zeng Y, Yu X, Liao B, Xia X, Yi P, Chu PK (2009) Label-free optical biosensor based on localized surface plasmon resonance of immobilized gold nanorods. Colloids Surf, B 71(1):96–101
6. Cinel NA, Bütün S, Özbay E (2012) Electron beam lithography designed silver nano-disks used as label free nano-biosensors based on localized surface plasmon resonance. Opt Express 20(3):2587–2597
7. Lee SW, Lee KS, Ahn J, Lee JJ, Kim MG, Shin YB (2011) Highly sensitive biosensing using arrays of plasmonic Au nanodisks realized by nanoimprint lithography. ACS Nano 5(2):897–904
8. Okamoto T, Yamaguchi I, Kobayashi T (2000) Local plasmon sensor with gold colloid monolayers deposited upon glass substrates. Opt Lett 25(6):372–374
9. Nazri N, Azeman NH, Bakar M, Mobarak NN, Luo Y, Arsad N, Aziz T, Zain A, Bakar A (2021) Localized surface plasmon resonance decorated with carbon quantum dots and triangular Ag nanoparticles for chlorophyll detection. Nanomaterials 12(1):35
10. Ryu KR, Kim GW, Ha JW (2021) Localized surface plasmon resonance inflection points for improved detection of chemisorption of 1-alkanethiols under total internal reflection scattering microscopy. Sci Rep 11(1):12902
11. Jeon HB, Tsalu PV, Ha JW (2019) Shape effect on the refractive index sensitivity at localized surface plasmon resonance inflection points of single gold nanocubes with vertices. Sci Rep 9(1):13635
12. Thomson CV (2012) Solid-state dewetting of thin films. Anny Rev Mater Res 42:399–434
13. Ozhikandathil J, Badilescu S, Packirisamy M (2012) Gold nanoislands integrated in a lab-on-a-chip for plasmonic detection of bovine growth hormone. J Biomed Opt 17(7):077001
14. Jia K, Bijeon JL, Adam PM et al (2013) Large scale fabrication of gold nano-structured substrates via high temperature annealing and their direct use for the LSPR detection of atrazine. Plasmonics 8:143–151
15. Ozhikandathil J, Packirisamy M (2014) Simulation and implementation of a morphology-tuned gold nano-island plasmonic sensor. Sensors 14(6):10497–10513
16. Bhalla N, Jain A, Lee Y, Shen AQ, Lee D (2019) Dewetting metal nanofilms-effect of substrate on refractive index sensitivity of nanoplasmonic gold. Nanomaterials 9(11):1530
17. Chung T, Lee Y, Ahn MS, Lee W, Bae SI, Hwang C, Jeong KH (2019) Nanoislands as plasmonic materials Nanoscale 11(18):8651–8664
18. Bendikov TA, Rabinkov A, Karakouz T, Vaskevich A, Rubinstein I (2008) Biological sensing and interface design in gold island film based localized plasmon transducers. Anal Chem 80(19):7487–7498
19. Tesler AB, Maoz BM, Feldman Y, Vaskevich A, Rubinstein I (2013) Solid-state thermal dewetting of just-percolated gold films evaporated on glass: development of the morphology and optical properties. The Journal of Physical Chemistry C 117(21):11337–11346
20. Barrios CA, Mirea T, Represa MH (2023) A self-referenced refractive index sensor based on gold nanoislands. Sensors 23(1):66
21. Hastings JT, Guo J, Keathley PD, Kumaresh PB, Wei Y, Bachas LS, LG, (2007) Optimal self-referenced sensing using long-and short-range surface plasmons. Opt Express 15(26):17661–17672
22. Srivastava SK, Verma R, Gupta BDJOC (2016) Theoretical modeling of a self-referenced dual mode SPR sensor utilizing indium tin oxide film. Opt Commun 369:131–137
23. Wang Y, Sun C, Li H, Chen GQ, J, (2017) Self-reference plasmonic sensors based on double Fano resonances. Nanoscale 9(31):11085–11092
24. Sharma AK, Pandey AKJB (2019) Self-referenced plasmonic sensor with TiO_2 grating on thin Au layer: simulated performance analysis in optical communication band. J Opt Soc Am B 36:F25–31
25. Sun P, Zhou C, Jia W, Xiang C, Xie Y, Zhao D (2020) Self-referenced refractive index sensor based on hybrid mode resonances in 2D metal-dielectric grating. J Phys D: Appl Phys 53:145101
26. Zhao M, Wang J, Zhang Y, Ge M, Zhang P, Li SJ, C, (2022) Self-referenced refractive index sensor based on double-dips method with bimetal-dielectric and double-groove grating. Opt Express 30(5):8376–8390
27. Malitson IH (1965) Interspecimen comparison of the refractive index of fused silica. J Opt Soc Am 55(10):1205–1209
28. Rakic AD, Djurisic AB, Elazar JM, Majewski ML (1998) Optical properties of metallic films for vertical-cavity optoelectronic devices. Appl Opt 37(22):5271–5283
29. Technical note. Drude dispersion model. Horiba. https://www.horiba.com/fileadmin/uploads/Scientific/Downloads/OpticalSchool_CN/TN/ellipsometer/Drude_Dispersion_Model.pdf
30. Suh CW, Kim MY, Choo JB, Kim JK, Kim HK, Lee EK (2004) Analysis of protein adsorption characteristics to nano-pore silica particles by using confocal laser scanning microscopy. J Biotechnol 112(3):267–277
31. Tsai DH, DelRio FW, Keene AM, Tyner KM, MacCuspie RI, Cho TJ, Zachariah MR, Hackley VA (2011) Adsorption and conformation of serum albumin protein on gold nanoparticles investigated using dimensional measurements and in situ spectroscopic methods. Langmuir 27(6):2464–2477
32. Kubiak-Ossowska K, Tokarczyk K, Jachimska B, Mulheran PA (2017) Bovine serum albumin adsorption at a silica surface explored by simulation and experiment. J Phys Chem B 121(16):3975–3986
33. Asanov AN, Delucas LJ, Oldham PB, Wilson WW (1997) Interfacial aggregation of bovine serum albumin related to crystallization conditions studied by total internal reflection fluorescence. J Colloid Interface Sci 196(1):62–73
34. Valle-Delgado JJ, Molina-Bolívar JA, Galisteo-González F, Gálvez-Ruiz MJ, Feiler A, Rutland MW (2004) Interaction forces

between BSA layers adsorbed on silica surfaces measured with an atomic force microscope. J Phys Chem B 108(17):5365–5371
35. Hwang Y, Ferhan AR, Yoon BK, Sut TN, Jeon WY, Koo DJ, Jackman JA, Cho NJ (2002) Surface engineering of plasmonic gold nanoislands for high-sensitivity refractometric biosensing applications. Appl Mater Today 26:101280
36. Anker JN, Hall WP, Lyandres O, Shah NC, Zhao J, Van Duyne RP (2008) Biosensing with plasmonic nanosensors. Nat Mater 7(6):442–453
37. Kedem O, Vaskevich A, Rubinstein I (2014) Critical issues in localized plasmon sensing. The Journal of Physical Chemistry C 118(16):8227–8244
38. Gao D, Chen W, Mulchandani A, Schultz JS (2007) Detection of tumor markers based on extinction spectra of visible light passing through gold nanoholes. Appl Phys Lett 90(7):2007
39. Hsiao A, Gartia MR, Chang TW, Wang X, Khumwan P, Liu GL (2015) Colorimetric plasmon resonance microfluidics on nanohole array sensors. Sens Biosens Res 5:24–32
40. Jackman JA, Ferhan AR, Yoon BK, Park JH, Zhdanov VP, Cho NJ (2017) Indirect nanoplasmonic sensing platform for monitoring temperature-dependent protein adsorption. Anal Chem 89(23):12976–12983
41. Zhao C, Xu X, Ferhan AR, Chiang N, Jackman JA, Yang Q, Liu W, Andrews AM, Cho NJ, Weiss PS (2020) Scalable fabrication of quasi-one-dimensional gold nanoribbons for plasmonic sensing. Nano Lett 20:1747–1754
42. Kumari S, Mohapatra S, Moirangthem RS (2017) Development of flexible plasmonic plastic sensor using nanograting textured laminating film. Mater Res Express 4:025008
43. Mariani S, Paghi A, La Mattina AA, Debrassi A, Dahne L, Barillaro G (2019) Decoration of porous silicon with gold nanoparticles via layer-by-layer nanoassembly for interferometric and hybrid photonic/plasmonic (bio)sensing. ACS Appl Mater Interfaces 11:43731–43740
44. Norde W, Giacomelli CE (2000) BSA structural changes during homomolecular exchange between the adsorbed and the dissolved states. J Biotechnol 79(3):259–268
45. Hägglund C, Zeltzer G, Ruiz R, Wangperawong A, Roelofs KE, Bent SF (2016) Strong coupling of plasmon and nanocavity modes for dual-band, near-perfect absorbers and ultrathin photovoltaics. ACS Photonics 3:456–463
46. Norde W (1996) Driving forces for protein adsorption at solid surfaces. Macromol Symp 103(1):5–18